CHAPTER II

Experiment: High Resolution, Direct Absorption, Infrared Spectrometer and Slit-Jet Cluster Source

2.1 Introduction

With any experimental apparatus that has been subjected to several generations of graduate students (I am either third or fourth, depending on what constitutes a "generation") a process of "experiment evolution" takes place. The fundamentals of the experiment remain, e.g., an infrared laser and a slit supersonic expansion, but the details of the implementation are continually improved upon. Arguably, my greatest experimental contribution as a graduate student has been the development of the slit-jet electric discharge, which is employed for generating cold molecular ions and radicals. However, since a detailed description of the slit-discharge is not required for understanding the work on small molecular clusters (Chapters 3 through 8), it is postponed until Chapters 9, 10 and the beginning of Chapter 11. Presented in this chapter is a description of the direct absorption infrared laser spectrometer and slit jet cluster source in their most recent incarnations. Since much of the experimental details have been described both in the literature[1-5] and in previous theses,[6-9] an overview approach is therefore adopted. Of course, areas of improvement that are not presented elsewhere are accordingly described in more detail.

The basis of the experiment is conceptually straight forward, i.e., pass a light source of a known color through a sample and measure, as a function of the light color, the attenuation via Beer's law:

$$A(\nu) = n\,\sigma\,l \qquad (2.1)$$

which relates the frequency dependent absorbance $A(\nu) = -\ln(I/I_0)$ to the number density n (molecules/cm^3), the pathlength l (cm), and the absorption cross section σ (cm^2). This inherent simplicity not only minimizes misinterpretations of the experimental results, but also, with known cross sections, permits the determination of absolute number densities. The combination of an ever increasing desire for enhanced spectroscopic detail and the limited number densities achievable for transient molecules, however, results in significant experimental challenges for implementing this simple idea. These challenges may be grouped into three categories, i) control of the light source, ii) generation of sufficient absorbance, and iii) suppression of noise. The remainder of this chapter is organized around these three groups, with a description of the experimental challenges and solutions for each group presented.

2.2 The High Resolution Difference Frequency Infrared Laser

This section describes the generation and calibration of the high-resolution, continuous wave, infrared laser used for all of the studies presented in this thesis. A schematic representation of the infrared spectrometer is shown in Figure 2.1. Before embarking on a detailed description of all the experimental

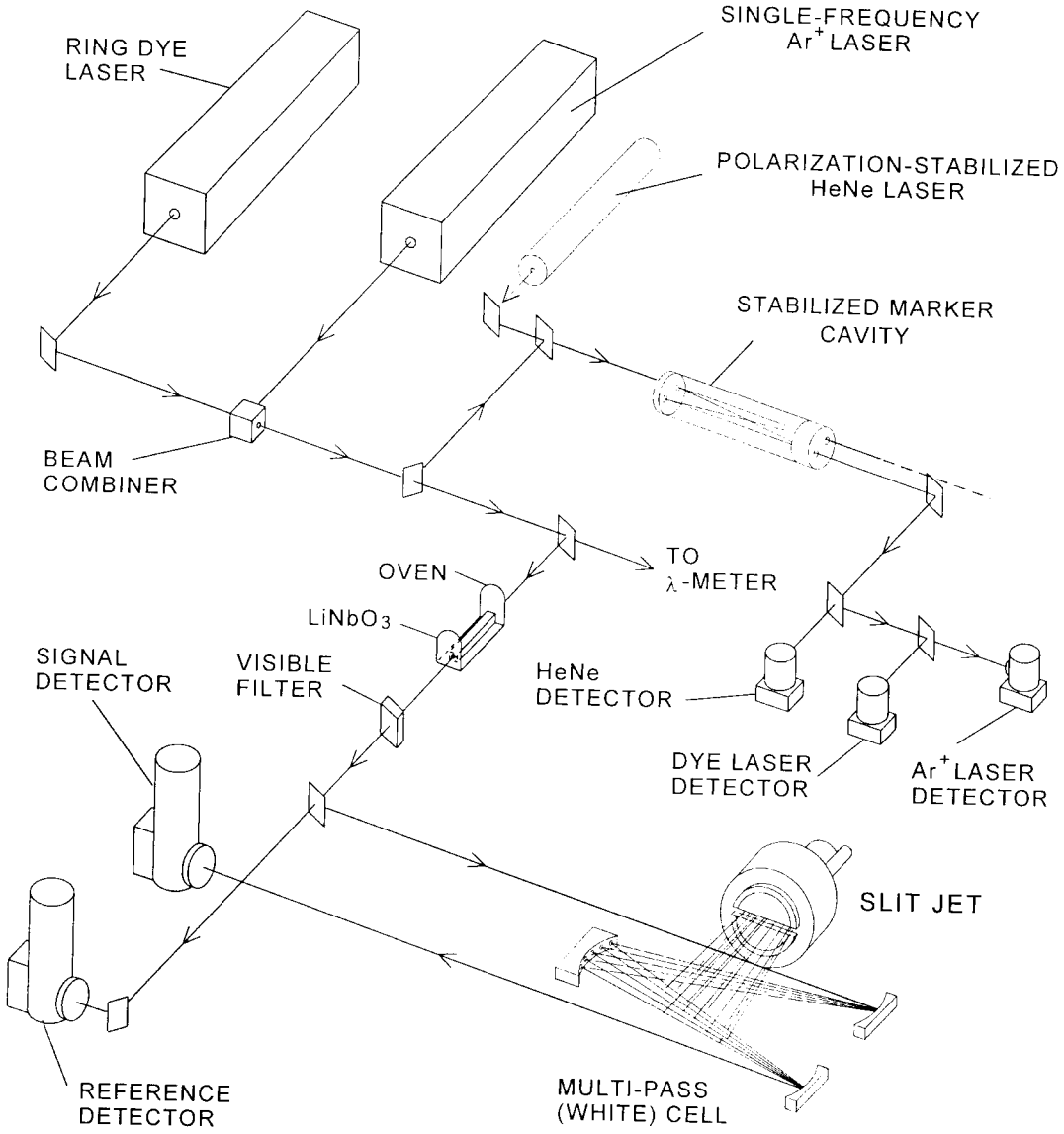

Figure 2.1 Schematic of the experimental apparatus used.

aspects portrayed in Figure 2.1, however, it is worth briefly mentioning some of the general advantages associated with spectroscopic investigations in the infrared.

In the interest of being able to probe a wide array of chemically interesting molecular species and dynamically interesting phenomena, the spectral region corresponding to typical vibrational energies of molecules, i.e. the infrared, offers some particular advantages. Unlike the pure rotational spectroscopy of the microwave region, the molecules investigated need not have a permanent dipole moment, but only exhibit a nonzero dipole moment derivative upon vibrational excitation. Furthermore, the presence of vibrational quanta introduces the possibility of dynamical investigation (IVR, predissociation, Fermi resonances, Coriolis coupling, etc...) typically not available in the microwave region. Additionally, vibrational excitation often accesses wavefunctions with significant amplitude in regions of the potential surface not sampled by the vibrational ground state. As a potential drawback, however, the resolution in the infrared region is fundamentally hindered by the increased Doppler broadening ($\Delta\nu \propto \nu_0$), with respect to the microwave region. While this is true, it is still sufficient (typically by orders of magnitude) to fully resolve rotational structure for even "large" molecules. In the visible and ultraviolet regions of the spectrum (electronic spectroscopy) this is frequently not the case, due to both increased Doppler broadening and often limited lifetimes for the electronic excited states, which in turn impedes structural characterization. While each spectral region offers specific advantages, far too many to mention in any detail here, the infrared

region is compelling due to the large number of molecules accessible, the possibility of interesting dynamical behavior, and the high, fully rotationally resolved, spectral resolution.

2.2.1 Nonlinear Difference Frequency Generation as an Infrared Laser Source

The choice of an infrared radiation source for spectroscopic investigations must balance, among other things, the desires for i) frequency coverage, ii) spectral resolution, and iii) ease of use. The infrared light used in these experiments is generated from nonlinear mixing of a tunable dye laser and a fixed frequency Ar^+ laser in a $LiNbO_3$ crystal. While other sources of infrared light, such as diode lasers and F-center lasers, provide substantially more power than the $\approx$10 μW achieved with the difference frequency technique, the broad spectral coverage (2.2-4.2 μm), high frequency resolution ($\Delta\nu \approx 2$ MHz), and good spatial characteristics of the difference frequency laser make it the more attractive light source for us. These favorable properties arise from the infrared generation via the mixing of two visible lasers. Characterization and conditioning of the visible lasers, therefore, translates directly into the infrared. This accounts for the ease of continuous scanning over hundreds of wavenumbers, through the spectral region that encompasses the chemically interesting C-H, N-H, O-H, H-F, H-Cl, stretches. This also greatly facilitates spectral searches for highly anharmonic *inter*molecular vibrations, where harmonic based theoretical predictions might be significantly in error.

The detailed underlying physics of nonlinear difference frequency generation have been described in detail elsewhere,[10,11] and hence only an extremely brief review is presented here. The origin of difference frequency generation (as well as the closely related three wave mixing phenomena of sum frequency generation, second harmonic generation, optical parametric amplification, etc..) arises from the nonlinear response of a dielectric polarization to an applied electric field. Specifically, the second term of a Taylor series expansion for the polarization of a dielectric medium as a function of applied electric field contains the product of two applied fields, i.e., the E^2 term. In the case of two sinusoidal applied electric fields at frequencies ω_1 and ω_2, the polarization will therefore have a component that oscillates at the sum and difference frequencies [$2 \sin(\omega_1) \sin(\omega_2) = \cos(\omega_1-\omega_2) - \cos(\omega_1+\omega_2)$]. This oscillating polarization subsequently creates an electromagnetic wave at the sum and difference of the two applied frequencies. Of course this is a classical representation, and ultimately at the quantum level, it is photons that are being destroyed and created.

As mentioned earlier, the infrared light at ω_3 is generated from the difference frequency of an Ar^+ laser at ω_1 and a dye laser at ω_2. Physically, the destruction of a high energy Ar^+ photon is accompanied by the generation of the energetically equivalent pair of the two lower energy dye and infrared photons, i.e.,

$$\omega_1 = \omega_2 + \omega_3 \qquad (2.2)$$

or equivalently,

$$\omega_3 = \omega_1 - \omega_2 \tag{2.3}$$

where these two equations simply reflect the constraint of conservation of energy.

The efficiency of this process can be greatly enhanced through the added constraint of conservation of photon momenta $n_i\omega_i$

$$n_3\omega_3 = n_1\omega_1 - n_2\omega_2 \tag{2.4}$$

where $n_i = k_i c/\omega_3$ is the index of refraction for the different frequencies. This is often expressed in terms of the wave vectors $\boldsymbol{k}_i$:

$$\Delta\boldsymbol{k} = \boldsymbol{k}_1 + \boldsymbol{k}_2 - \boldsymbol{k}_3 = 0 \tag{2.5}$$

and refereed to as "phase matching", since the requirement of equation (2.5) corresponds to the experimental condition where the difference frequency wave maintains a fixed phase relationship with respect to the incident waves. The experimental technique for maintaining optimum phase matching will be described below.

The specific cw lasers used for difference frequency generation are a spectra physics 380 ring dye laser (with Rhodamine 6G used for all experiments) and a single frequency Spectra Physics model 2020 Ar^+ laser. It should be noted that this experimental technique is based on the method developed by Alan Pine.[12] The dye laser cavity is in a ring configuration to eliminate spatial hole burning and actively stabilized ($\Delta\nu \approx 1$ MHz) to an external fabry perot etalon, as discussed in more detail in the next subsection. Additionally, the stainless steel dye nozzle has been replaced by a sapphire nozzle, which provides a much more stable and uniform dye jet. Typical dye pressures behind the jet range from 90 to 120 psi. The dye laser is housed in a flow hood equipped with a blower module

(Laminaire model LP-24) which provides a continuous flow of filtered air. This greatly reduces the frequency with which the intracavity optics need to be cleaned. The dye laser is pumped by approximately 5 Watts from an all lines Ar^+ laser (Spectra Physics model 2020). Typical dye powers range from 0.3 to 0.5 watts. The single frequency Ar^+ laser used for the difference frequency generation is also a Spectra physics model 2020, but with the addition of a prism (to select one atomic transition, either the 488 or 514 nm line) and a temperature stabilized intracavity etalon (to select a single longitudinal mode).

These two lasers are polarized orthogonal to one another, rendered collinear via a polarization combining cube, and focused by an achromatic doublet into the center of the 5 cm long $LiNbO_3$ crystal. Phase matching is achieved by exploiting the different rates at which the index of refraction of the extraordinary and ordinary axes of the crystal tune with temperature. The crystal orientation is aligned such that the extraordinary axis is aligned 90° with respect to the Poynting vector of the incident beams (90° phase matching). This method, as opposed to angle tuning, permits phase matching throughout the 5 cm length of the crystal. Since difference frequency generation scales with the square of the pathlength,[10] this technique permits infrared generation even with the relatively weak cw laser sources used. The draw back of this technique, however, is the need to stabilize the crystal temperature to 1 part in 10^4.

The $LiNbO_3$ crystal is housed in a JILA machined oven core. The core is made from two pieces of copper, which when put together (alignment achieved by machined pins and holes), make a cylindrical object with an approximate 4.5×4.5

mm square hole throughout the center where the crystal resides. A drawing of the oven core is shown in Figure 2.2. The numbered steps indicated in the drawing are for windings of 28 gauge fiberglass insulated NiChrome heater wire. Each step of the core is non-inductively wound with five turns of the heater wire, for a total of forty windings. A small hole in the center of the oven core is utilized for placement of an iron-constantine thermocouple. Care must be taken to avoid any electrical connection between the oven core, heater wire, and/or thermocouple wire. The oven core/heater winding/thermocouple combination is encased in Sauereisen (a high temperature ceramic) to provide structural stability. The oven core is suspended in an external housing via two cylindrical quartz spacers. The volume between the core and housing shell is filled with an insulator to reduce air flow and potential thermal instabalities. A slow flow of oxygen is provided to the oven core through the faceplates of the outer housing to counter the thermally driven reduction of $LiNbO_3$. The copper oven core is gold plated to reduce oxidation.

The temperature of the oven core is measured via the attached thermocouple, the output from which is conditioned and converted to an analog output voltage in a chopper-stabilized, cold-junction compensated, isolated thermocouple input module (Burr-Brown Model SCM5B). This output is compared to a request voltage, and the resulting error signal is utilized to either increase or decrease the duty cycle with which the crystal is heated. For details of

$LiNbO_3$ Oven Core

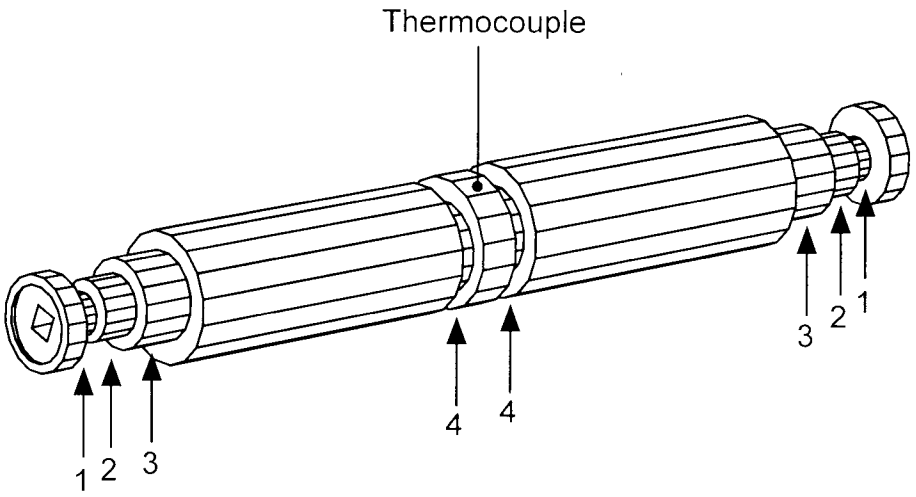

Figure 2.2. A drawing of the gold plated, copper, $LiNbO_3$ oven core. The 4mm×4mm ×5cm crystal slides through the rectangular hole into the center of the oven core. This cores is subsequently suspended, via quartz spaces, in the oven housing. The numbered regions indicated in the drawing specify where heater wire is wound. The greater number of windings at the end of the oven core help offset the cooling at the edges.

this circuit the reader is referred to Ref. 6. As the dye laser, and hence the infrared laser, is scanned the temperature of the crystal must be tuned to retain phase matching. This is accomplished by simultaneously scanning the request voltage. This technique has proven sufficient to maintain ±0.02 °C temperature stability over the 200-500 °C range required for 2.2-4.2 μm generation.

2.2.2 Infrared Frequency Stabilization and Calibration

The spectral demands on the infrared laser source required for the work presented in this thesis may be grouped into two catagories. First, in the interest of resolving subtle broadening effects (due to predissociation, fine structure, etc.) the frequency jitter needs to be minimized. Second, a means of accurately calibrating the relative frequency difference between absorption peaks is required. This second demand is particularly challenging since data collection for the frequently large regions scanned requires significant time (often > 24 hours), and therefore any frequency drift on the time scale of days will limit the precision of the data. Since the infrared light is generated from two visible lasers, the easier task of stabilizing and calibrating the visible sources is employed. Specifically, the frequency jitter of the infrared light is provided by the uncorrelated sum of squares of the frequency jitter of the two visible lasers:

$$\Delta\nu_{IR} = \sqrt{\Delta\nu_{dye}^2 + \Delta\nu_{Ar^+}^2} \tag{2.6}$$

Therefore, minimization of the visible laser frequency noise will subsequently minimize the noise in the infrared. Likewise, accurate determination of the length of frequency scanned is provided by the combination of i) determination of the frequency scanned by the dye laser and ii) minimization of frequency drift in the Ar^+ laser. A schematic of the optics associated with achieving these goals is displayed in Figure 2.3.

As with any calibration or measurement scheme, a standard against which to judge the desired quantities is necessary. For the laser frequency stability, both

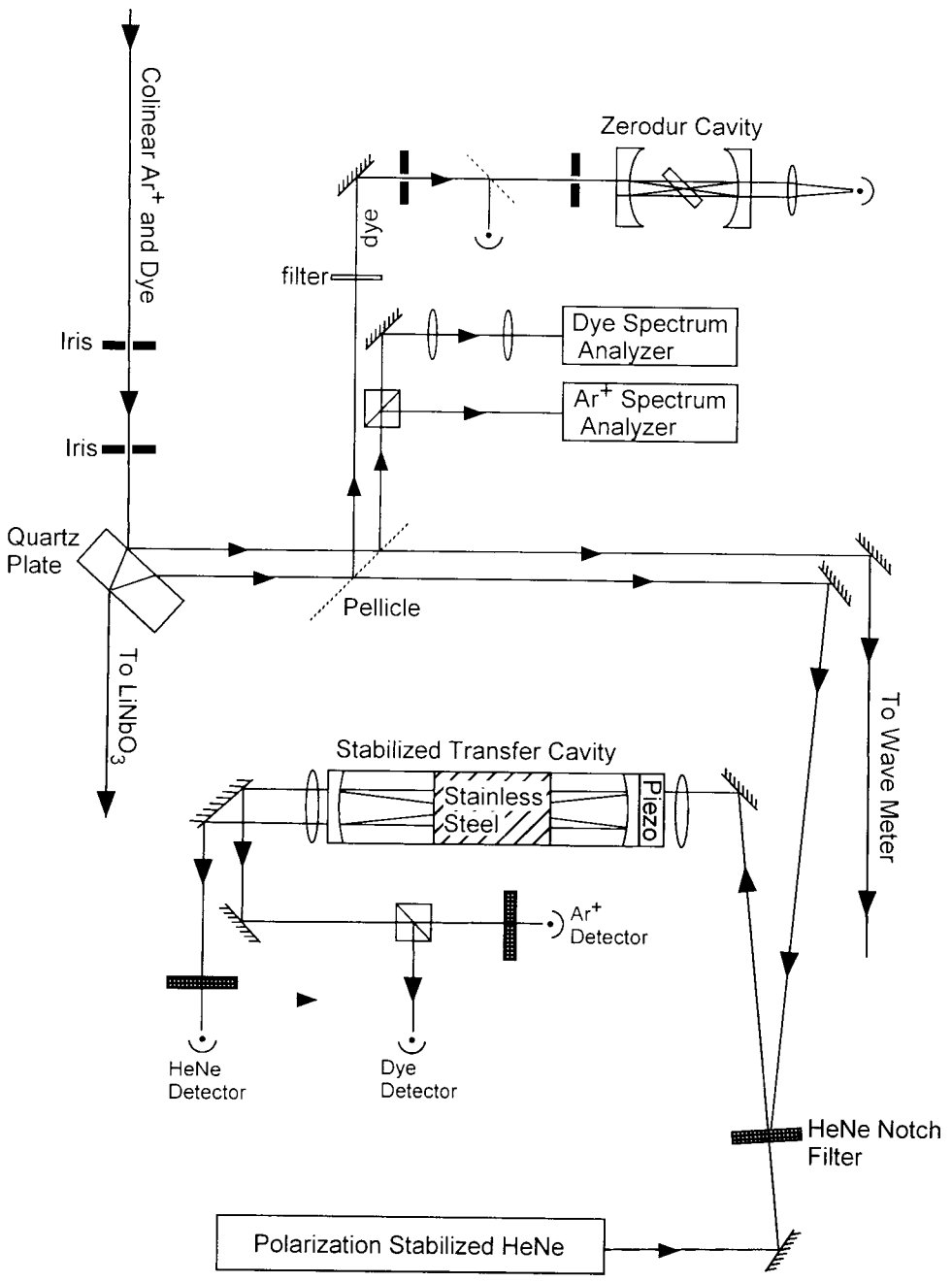

Figure 2.3 A schematic of the optical path, stabilized cavities, and spectrum analyzers utilized to condition the two visible and therefore the infrared laser beam.

long and short timescales, a convenient standard is provided by a polarization stabilized helium neon laser.[13,14] This is a homebuilt laser, utilizing a commercially available 0.5 milliwatt, unpolarized (Uniphase model # 1008) helium neon laser tube. Unavoidable birefringence in the cavity optics results in the simultaneous lasing of two, orthogonally polarized, longitudinal modes. As described in more detail elsewhere,[9] stabilizing the intensity ratio for these two modes, via heating and cooling of the laser tube, results in a remarkably stable light source. Through optical mode beating with a Lamb dip- iodine- stabilized HeNe laser,[15] the short (< 0.1 MHz/hr) and long term (< 2 MHz over days) stability of this source has been established.

An experimental means of transferring the optical stability of the HeNe laser described above to the other light sources is required. This is achieved through the use of a specially designed Fabry Perot confocal etalon.[4] As qualitatively depicted in Figure 2.3, this "transfer cavity" is a 30 cm long Fabry-Perot Interferometer (free spectral range of 250 MHz) constructed of two pyrex, one stainless steel, and one piezo section. Heating and cooling of the stainless steel section allows for large, albeit slow, changes in the cavity length, while application of voltage to the piezo cylinder permits, fast, albeit small, changes in the cavity length. The stabilized HeNe beam is passed through this cavity and the length of the cavity is then locked to a transmission fringe of this HeNe beam. Specifically, a 4.4 KHz dither is applied to the piezo voltage, and then phase sensitive lock-in detection techniques (at 2ω = 8.8 KHz local oscillator frequency consistent with a "top lock") on the transmitted HeNe laser light (as measured on

a photodiode) permit generation of an error signal. Minimizing this error signal maintains the *optical* length of the cavity. It is worth noting that the physical length of the cavity may change substantially, as air pressure and room temperature change, but it is the stability of the optical and not the physical length which is of concern to us. Repeated scans over the same molecular transitions have demonstrated the optical stability of the cavity at less than or equal to a few MHz. For the 30 cm cavity used this translates into a stabilization of the optical path length at the level of a few Angstroms, which makes for a remarkably useful "optical ruler".

With the stabilized transfer cavity described above, the tools for both decreasing the frequency jitter and effectively eliminating the long term drift of the Ar^+ laser are now in place. Specifically, one of the end mirrors for the Ar^+ cavity is mounted on a piezo disk, which allows for scanning of the cavity length and therefore the laser frequency. A small piece of the Ar^+ beam is sent through the "transfer cavity", and subsequently detected via a photodiode. A lock-in detection scheme analogous to what was described above, utilizing the already present dither on the transfer cavity piezo, permits locking the Ar^+ frequency to correspond to a transmission fringe of the stabilized cavity. This not only decreases the frequency jitter of the Ar^+ laser by an order of magnitude (from $\approx$10 MHz to $\approx$1 MHz), as measured by the spectrum analyzer indicated in Figure 2.3, but it also reduces the long term drift to a negligible level.

Stabilization of the ring dye laser is accomplished through a "side lock" technique, where a small portion of the dye beam is transmitted through a 10 cm

long zerodur Fabry-Perot etalon (in a bowtie rather than coaxial arrangement to minimize optical feedback). For a fixed optical length of this zerodur cavity, the intensity of the dye beam transmitted through this cavity is a function of the dye laser frequency. Adjusting the dye laser frequency (via an intracavity etalon, intracavity galvo plates, and a piezo mounted mirror) to keep the transmission maintained at a set value therefore results in also fixing the dye frequency. To compensate for misinterpreting dye power fluctuations as frequency fluctuations, the ratio of the transmitted dye power to an independent measure of the total dye power is therefore used. This active stabilization reduces the dye laser frequency jitter (arising largely from acoustic fluctuations in the dye jet) to the ≈1 MHz level, as measured on a spectra physics spectrum analyzer. Of course, the long term stability of this zerodur cavity is considerably worse than the optical transfer cavity described above, but since the dye laser is scanned it is not a question of long term stability but rather a question of calibrating the magnitude of the frequency region scanned.

Since the dye laser is locked to the zerodur cavity, changing the optical length of the cavity therefore changes the frequency the dye laser is locked to. This is accomplished via a stepwise rotation of a quartz plate mounted inside of the zerodur cavity. Simultaneously, a feed forward signal is sent to the dye laser's intracavity etalon and galvo plates in order to "track" the scanning. The magnitude of the frequency step is determined by the degree of attenuation of a computer generated 0-5 volt ramp (divided into 4096 steps). Typical scan steps vary from 1-2 MHz for lineshape analysis at the small end, and up to ≈15 MHz at

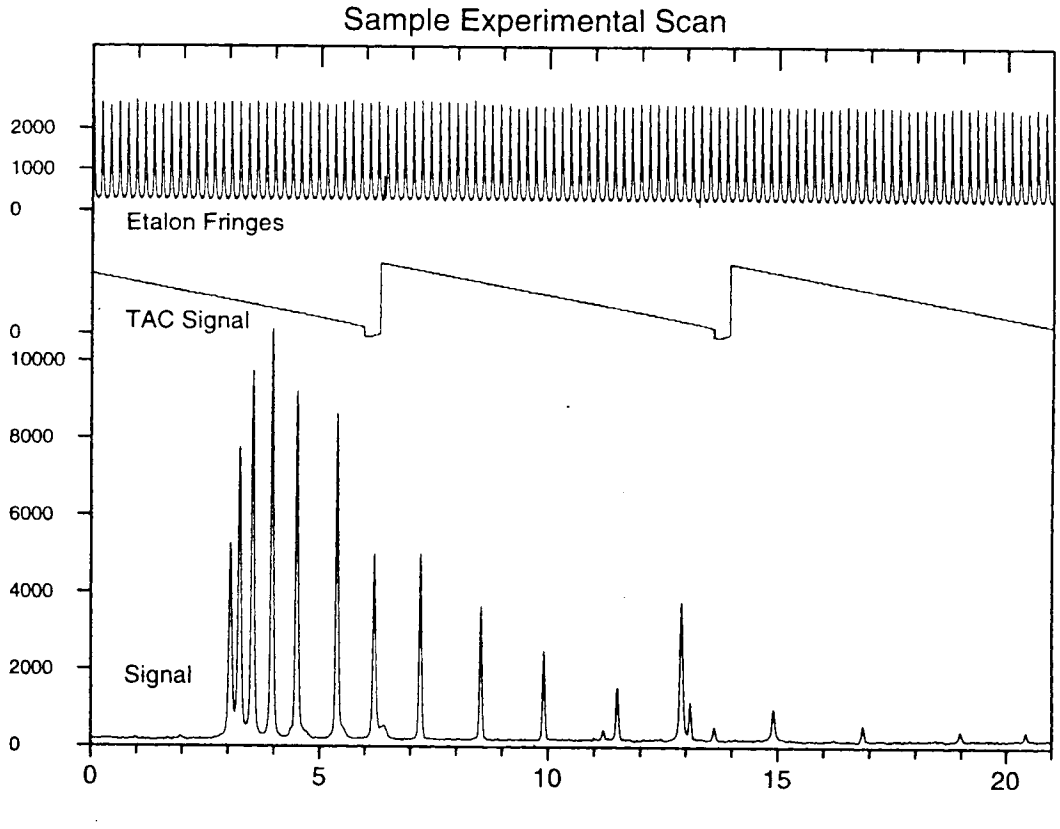

Figure 2.4 A sample data scan displaying the TAC, etalon, and infrared absorption (in this example a Q-branch of HF dimer). This figure is an example of "raw" data prior to linearization, and therefore the values on the x-axis represents arbitrary numbers.

the large end for scanning wide spectral regions. As the dye laser is scanned, a small percentage of the laser is sent through the stabilized transfer cavity. Recording the transmission fringes then permits a linear interpolation between etalon peaks, which are separated by a known free spectral range, and therefore allows an accurate conversion from data point to relative frequency scanned. Furthermore, the spectrum analyzer is also used during the course of the dye laser scan to verify mode-hop-free operation. This is accomplished via the use of a time to amplitude converter (TAC) on the photodiode signal from the back of the spectrum analyzer. As the length of the spectrum analyzer is swept, the time required for the photodiode voltage to reach a preset level is converted to a voltage and stored. As the dye laser scans, this arrival time changes with respect to the beginning of the spectrum analyzer sweep, which leads to an incrementing voltage ramp. Displayed in Figure 2.4 is a sample data scan. At each laser step the infrared absorbance, TAC signal, etalon fringes, and IR power (not shown) are saved. The process of concatenation of several smaller scans to make one large continuous scan is discussed below.

2.2.3 Absolute Frequency Calibration

With the relative frequencies between observed molecular transitions determined to within a few MHz, the problem of discerning the absolute absorption frequencies presents itself. One possible experimental method is to utilize a travelling Michelson-Morley interferometer, commonly referred to as a

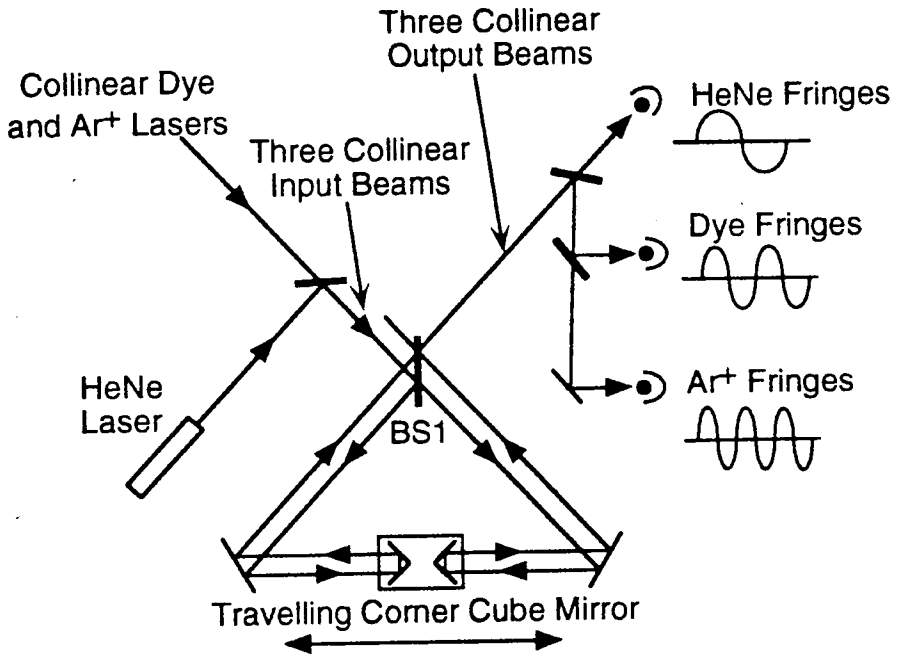

Figure 2.5 The 3-color travelling Michelson interferometer (wave meter)

wavemeter or simply a λ–meter.[16,17] This device, schematically shown in Figure 2.5, exploits the small Doppler shift induced for a laser reflecting off a moving mirror, in this case a corner cube mirror moving on an air track. The magnitude of this Doppler shift is dependent on both the frequency of the light and the velocity of the mirror. Since the mirror velocity is necessarily small with respect to the speed of light the Doppler shift may be expressed as:

$$\frac{\Delta \nu}{\nu_{laser}} \approx \frac{v_{cart}}{c} \tag{2.7}$$

The arrangement employed (see Figure 2.5) takes advantage of this Doppler shift by "beating" or "heterodyning" the red and blue shifted components of the same unknown laser frequency against one another. Since the Doppler shifts are small the resulting "beat note" (i.e. the difference between the frequency of the two components, which is just twice the Doppler shift for one of them) is subsequently within the realm of electronic counters. Measurement of this "beat" frequency, coupled with knowledge of the cart velocity, therefore provide the unknown laser frequency. In practice, however, determining the cart velocity to sufficient accuracy is prohibitively difficult, therefore we turn to our "spectral standard" of the polarization stabilized HeNe laser.

As shown in Figure 2.5, in addition to the two lasers with unknown frequencies (i.e. the dye and Ar^+) the HeNe laser with a known frequency is also sent, along the exact same optical path, through the wavemeter. One could think of this as utilizing the known frequency to calibrate the velocity of the cart. In practice, however, a fringe counting scheme is employed. Specifically, zero crossings of the ensuing interference fringes from each laser are counted, and the ratio of unknown laser fringe counts to known laser fringe counts provides the ratio of the laser wavelengths. The counting of fringes for all three lasers continues until a preset number of HeNe fringes is reached. Since this duration of time (or equivalently length of cart travel) will not correspond to an integral number of Ar^+ and dye fringes, errors will arise from not appropriately accounting

for the fractional fringe. This is reduced through a ×16 phase-locked loop multiplier, which exploits that fact that the cart velocity does not change rapidly and therefore can be extrapolated, based on the frequency of past fringes, to estimate the fraction of the final fringe. This interferometer provides the frequencies of the Ar^+ and dye lasers with a precision of 0.001 cm^{-1}. The accuracy, however, is limited by a number of factors.

The high precision of the wavemeter is not a measure of the absolute accuracy. Issues such as dispersion effects in air, and differing pathlengths for the lasers through the interferometer result in an absolute accuracy of only ≈ 0.05 cm^{-1}. For the purpose of determining the absolute frequency of an absorption in the supersonic jet, this can be further complicated by nonorthogonal crossing of the probe laser and the supersonic expansion axis. Especially for fast expansions in hydrogen and helium, this effect can not be ignored. A simple alternative, however, is to make use of the excellent relative precision of the spectrometer through coexpanding small quantities of a reference molecule. The absolute accuracy of the frequency measurements are then limited only by our high relative precision and the accuracy of the reference molecule.

While the wavemeter is not desirable for absolute frequency determination, the high precision achieved can often be utilized elsewhere. One particularly useful example is the process used for concatenating different spectral scans into one continuous scan. Lamda-metering one of the transmission peaks for the dye laser through the stabilized transfer cavity in each spectral scan permits unambiguous counting of fringes between scans. This in turn allows an

unambiguous concatenation, even for non overlapping scans. Additionally, this concatenation procedure does not propagate errors when a long series of scans are involved.

2.3 Increasing the Absorbance

2.3.1 Population per Quantum State

An essential element for direct absorption infrared studies, in addition to the generation and calibration of the infrared laser source described above, is, of course, a sample that provides sufficient absorption to detect above the noise. Following Beer's law (eq. 2.1), a direct and obvious approach for increasing absorption is to increase the sample density. In one extreme, molecules trapped in inert condensed phase liquid or solid environments provide extremely large densities and subsequently large absorptions. However, interactions between the chromophore and the environment not only complicate theoretical modeling but typically wash out any rotational structure. In the other extreme of low pressure cells, the densities, especially of weakly bound species, are often prohibitively small. This problem is further compounded by room temperature conditions, which dilutes the population over many thermally accessible rotational and/or vibrational states, thereby further decreasing the number density per quantum state. A long appreciated alternative to these two extremes has been to exploit the low translational (0.1 – 20 K) temperature produced by the adiabatic expansion of

gas into a vacuum. The subsequent reduction in the vibrational and rotational partition functions, via collisional energy transfer, greatly reduces spectral congestion and enhances the number density per quantum state for the few energy levels populated. Furthermore, the average kinetic energies associated with binary collisions in this cold environment are insufficient to rupture weakly bound molecular clusters, and therefore greatly enhance their relative abundance.

The advantages for direct absorption investigations of weakly bound clusters associated with a supersonic expansion (even modest pressure differentials, i.e. approximately > 2, between the stagnation and vacuum regions will result in supersonic flow) can be further enhanced through shaped expansions. Exploited in this thesis are the benefits associated with a *slit*, supersonic expansion. A cross sectional view of the JILA built slit-jet source is displayed in Figure 2.6. A detailed description of the source, along with the associated fluid dynamics appropriate for a slit expansion, are presented in the thesis of Chris Lovejoy.[9] The slit length is 4 cm and the width is adjustable from 60 to 400 μm. In addition to the obvious advantage over a pinhole expansion of increased pathlength, the density as a function of distance from the expansion orifice (R) varies as $1/R$ rather than the $1/R^2$ dependence for a pinhole geometry. Since cluster formation is a many body process, i.e., not only are the constituent species of the cluster required but also a third body to carry away excess energy, the increased density and therefore increased collisions provided by the slit greatly enhance this unlikely process. Further benefits associated with Doppler compression are discussed later.

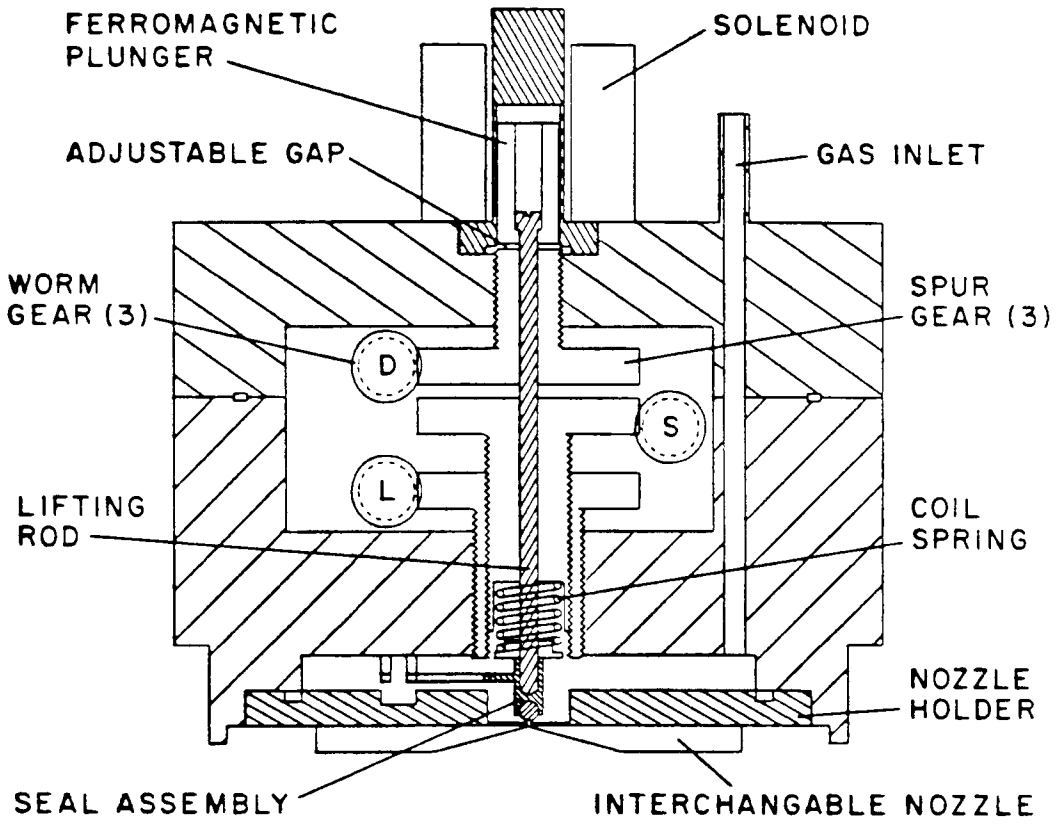

Figure 2.6 The pulsed slit valve utilized for cluster generation

The specific experimental flow conditions, i.e. backing (stagnation) pressure, diluent composition, and chromophore concentration, vary depending on the desired molecular species. Largely, however, 500-700 Torr backing pressures of gas composed of >99% inert atomic gases (Ar, Ne, or Helium) is utilized. The HF, HCl, or DF chromophore are kept at the < 1% level to prevent undesired "over clustering" to larger species. Premixes of the desired chemical composition can be made ahead of time and then flowed through the valve. Alternatively, gases may be mixed "on the fly" through either needle valves with flow meters (Tylan Model FM380) or flow controllers (Tylan Model FC280S). Typical flow rates are on the order of one standard liter per minute (slm). The vacuum pumps employed are a 1,342 cubic feet per minute (cfm) air cooled roots blower (Leybold model WS2000) backed by a mechanical, water cooled roughing pump (Kinney model KT-150).

The experimental difficulty with generating a specific cluster size arises, in part, from a tendency toward over clustering. This is demonstrated in Figure 2.7, which shows temporal absorption profiles for ArDF as a function of backing pressure (0.3% DF in Ar). At low pressure, the ArDF absorbance is relatively constant during the 700 μs duration that the pulsed valve is open. At consecutively higher backing pressures, the absorbance decreases during the central portion of the gas pulse, which corresponds to a higher density temporal region due to complete opening of the pulsed valve. The higher density gives rise to enhanced clustering, resulting in the conversion of the binary ArDF complex to larger $Ar_m(DF)_n$ (m,n > 2) complexes and therefore decreased absorption on

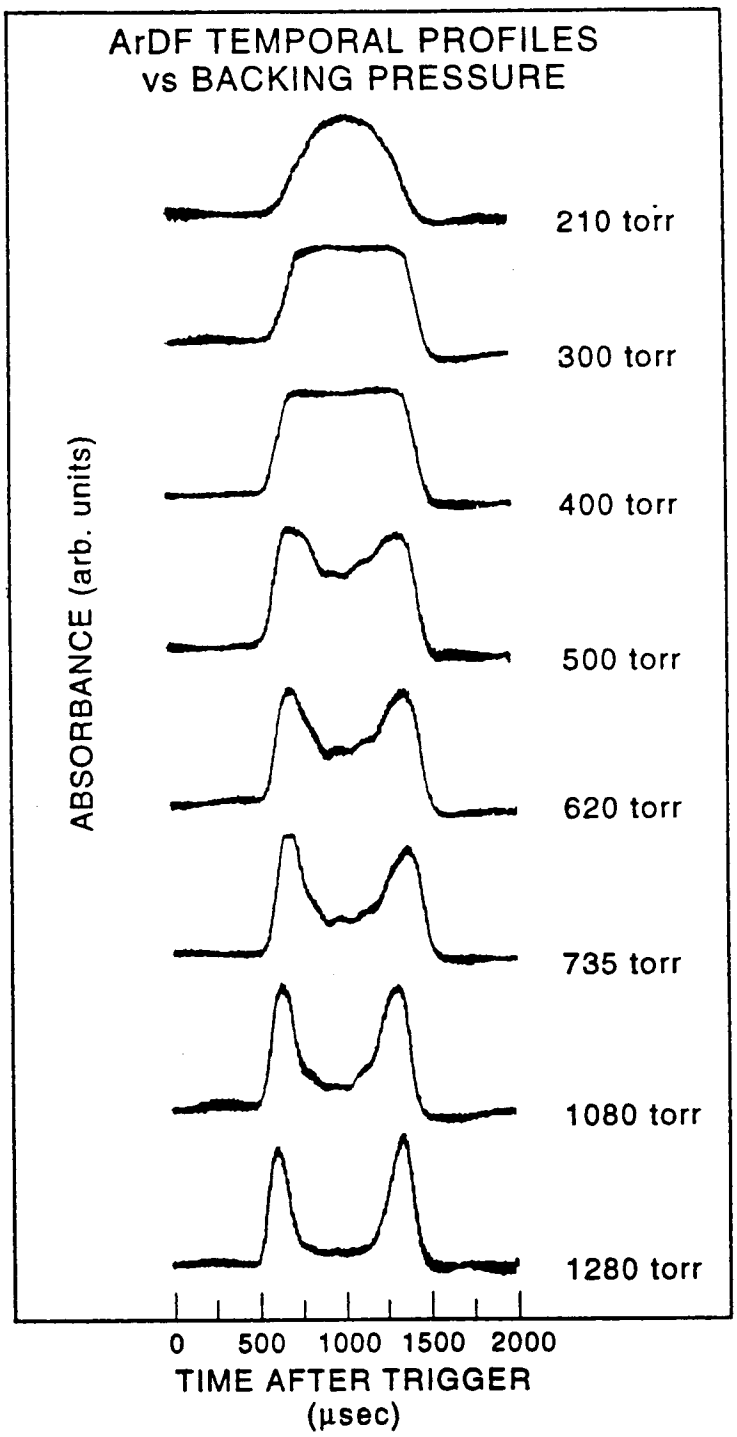

Figure 2.7 The temporal absorption profiles of ArDF as a function of backing pressure

ArDF. The pressure, and therefore density range, over which this conversion to higher clusters takes place is relatively narrow (e.g., only ≈100 torr difference for optimization of ArDF vs Ar_3DF). It is worth mentioning that while nearly complete depletion of monomer absorption with increased backing pressure can be achieved (indicating nearly 100% clustering), the amount relegated to the simple binary complexes is at most only 0.01%. Of course, even this modest "size specific" clustering efficiency allows high S/N spectral scans over the binary (S/N > 1000:1) and higher order complexes.

In addition to the rotational cooling provided by a supersonic expansion, the constraints of the slit geometry result in an equally important translational cooling for motion directed along the slit axis. Just as the rotational cooling collapsed the population into the low energy rotor levels, the translational cooling reduces the velocity spread for motion along the slit axis. This has the dual advantage of both increasing the experimental resolution through a reduction of Doppler broadening, and the resultant increase in absorption on line center for the same area under the curve Doppler profiles. This increased resolution permits sensitive detection of subtle broadening due to vibrational predissociation. To understand the limits of the experimental capabilities it is useful to consider the instrumental lineshape, as determined from high resolution scans over a known stable molecule.

The lifetime for the vibrationally excited ArDF binary complex has been established via a direct time of flight technique to be larger than 0.4 ms.[18] Since this extreme metastability eliminates any contributions from predissociation

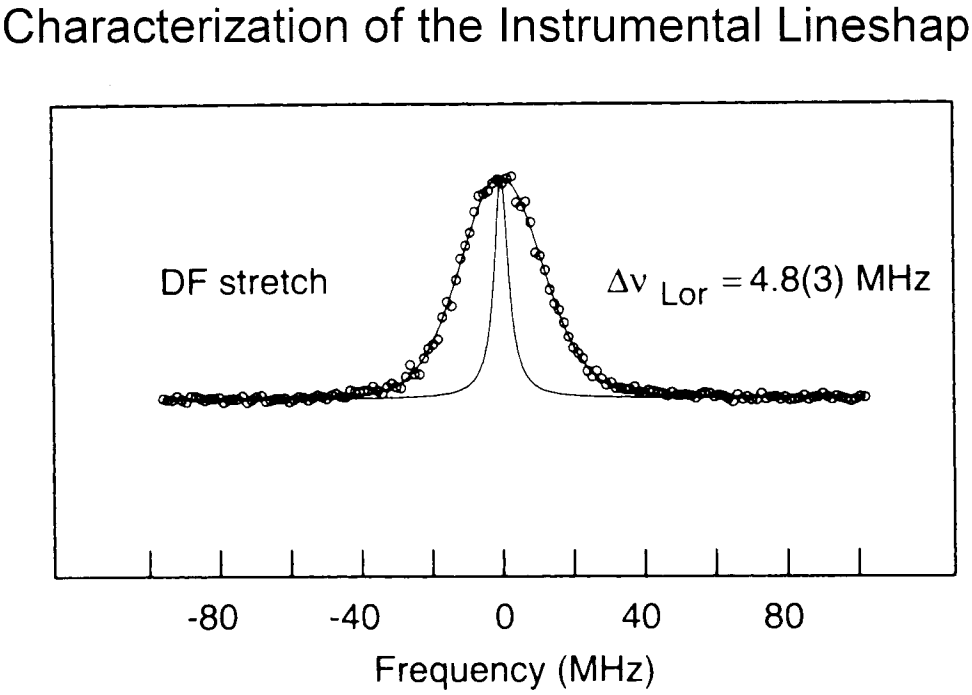

Figure 2.8 An experimental scan over a single rovibrational transition in ArDF. Plotted in circles are the experimental data, and the solid line running through the circles is a Voigt convolution of a Gaussian and Lorentzian. Shown separately, also as a solid line, is the Lorentzian contribution.

broadening to the lineshape, an analysis of an individual rovibrational transition (see Figure 2.8) yields direct information about instrumental contributions to the lineshape.

The contributions to the broadening of a line shape are conveniently split into homogenous and inhomogenous parts. Homogenous broadening processes include transit time broadening, pressure broadening, power or saturation broadening, and broadening due to laser frequency jitter. Inhomogenous broadening contributions arise from Doppler shifts due to the finite length of the

slit, nonorthogonal laser-molecular beam crossing, and the residual velocity distribution in the expansion.

We can readily estimate upper limits to line width contributions for each of the homogenous broadening processes. Transit time broadening can be estimated to be < 0.1 MHz from the molecule's velocity, 5.5×10^4 cm/sec (appropriate for an Ar expansion), and the size of the probe region, ≈ 0.1 cm laser diameter. The effect of pressure broadening can be estimated from pressure broadening coefficients for the hydrogen halides perturbed by rare gases,[19] and contributes < 0.01 MHz to the linewidth. Since the infrared laser source (< 10 μW) has quite low power, saturation broadening is negligible, estimated to be < 0.08 MHz. As discussed earlier in this chapter, the frequency jitter on the infrared light is approximately 2 MHz, considerably dominating all of the other instrumental sources of homogenous broadening.

Corresponding inhomogenous contributions can arise from a variety of sources. One possibility, for the ArDF transition displayed, that can be readily dismissed is unresolved hyperfine structure due to the deuterium quadrupole splittings. Predictions based on observed ArDF hyperfine data from microwave spectroscopy[20] predict this additional hyperfine structure at < 0.2 MHz level, i.e., negligible compared with other sources to be considered. For example, at room temperature Doppler line widths for DF (v = 1←0) are on the order of several hundreds of MHz. This velocity broadening is greatly diminished by employing a slit expansion geometry, where in zeroth order the observed Doppler line shapes are well characterized by a Gaussian profile, with a FWHM equal to that predicted

from the observed 10 K rotational temperature of the expansion. Additional Doppler shifts occur at the extreme edges of the slit where the gas expansion is unconstrained along the laser axis. However, since the aspect ratio for the slit is quite large (400:1), this effect broadens the sub-Doppler instrumental profile by a negligibly small amount. A more important source of Doppler broadening is induced by multipass optics, which for the slit geometry does not permit the laser axis to be perfectly orthogonal to the expansion direction, resulting in the stream velocity having a nonzero projection along the laser axis. Both the edge and nonorthogonal crossing effects can be reduced by slowing the stream veolicty, which is accomplished by increasing the mass of the diluent (e.g. Ar vs. Ne vs. He). With an Ar diluent, the observed Doppler broadening for ArDF complexes is ≈30 MHz, which is within 5% of the predicted residual transverse Doppler width in the 10 K expansion.

The net effect of these homogeneous and inhomogeneous contributions is to yield an instrumental line shape that is predominantly Gaussian due to residual Doppler broadening but with a much smaller component due to IR frequency noise. This minor second component is not as strongly peaked as the Doppler component, and thus contributes predominantly in the 'wings' of the Gaussian. Although there are many possible mathematical representations of the resulting instrumental line shape, a particularly appropriate choice is a Voigt convolution of a narrow Lorentzian ($\Delta\nu_{Lor.}^{instr.}$) over a predominantly Gaussian ($\Delta\nu_{Gau.}^{instr.}$) profile. This Voigt convolution offers the important mathematical advantage that the extraction of the additional homogeneous broadening due to vibrational

predissociation ($\Delta\nu_{prediss.}$) is particularly convenient. Specifically, it can be easily shown that the convolution of a second Lorentzian from vibrational predissociation over the instrumental Voigt profile yields another Voigt profile, with the same Gaussian component, and a net Lorentzian component which is simply the sum of $\Delta\nu_{prediss.}$ and $\Delta\nu_{Lor.}^{instr.}$. Thus, we can analyze both predissociating and nonpredissociating line widths with the same Voigt procedure, and isolate the predissociating contribution by subtraction.

Figure 2.8 displays the high resolution (1.4 MHz step size) experimental scan over a non predissociating ArDF vibration-rotation transition. The experimental lineshape (circles) is well reproduced by the Voigt model (solid line). While substantially smaller than the 30 MHz Gaussian contribution, the 4.8 MHz Lorentzian contribution is nevertheless substantially larger than estimates from the infrared laser noise. Indeed, this was originally interpreted as evidence for vibrational predissociation,[21] and points toward possible unaccounted for instrumental contributions to the lineshape. It is worth stressing, however, that this instrumental contribution is significantly smaller than the vibrational predissociation contribution (as large as 300 MHz) observed for the hydrogen bound dimers.

2.3.2 Increasing the Path Length

Functionally equivalent to increasing the absorber density, increasing the optical path length is a convenient means for enhancing infrared absorbance. In addition to the already mentioned dramatic increase provided by the slit vs. pinhole expansion geometries, multipass optics provide the opportunity to further multiply this enhancement by factors of ten to twenty. The two optical multipass configurations employed in these studies are the White cell[22,23] and the Herriott cell[24-26] (see Figure 2.9), with typical number of passes for both arrangements being 16, and therefore a total pathlength along the 4 cm slit of 64 cm.

In the White cell, the front and rear mirrors are separated by their radius of curvature. The laser is passed through appropriate lenses to focus the beam exactly at the front mirror, which minimizes clipping upon entering the cell. The optical arrangement for the White cell refocuses the laser on this front mirror with each pass, and therefore facilitates a clean exit from the cell. The Herriott cell on the other hand consists of two identical spherical mirrors seperated, very nearly but slightly less than twice the radius of curvature. Unlike the White cell, the incoming laser is focused at the center of the cell, rather than at the entrance mirror. Successive passes through the cell refocus the beam in the center. Since the laser does not come to a focus upon entrance and exit from the cell, the White cell might seem more convenient for minimizing clipping with increased number of passes. Two factors, however, prove this to be incorrect, as dicussed below.

Multipass Optics

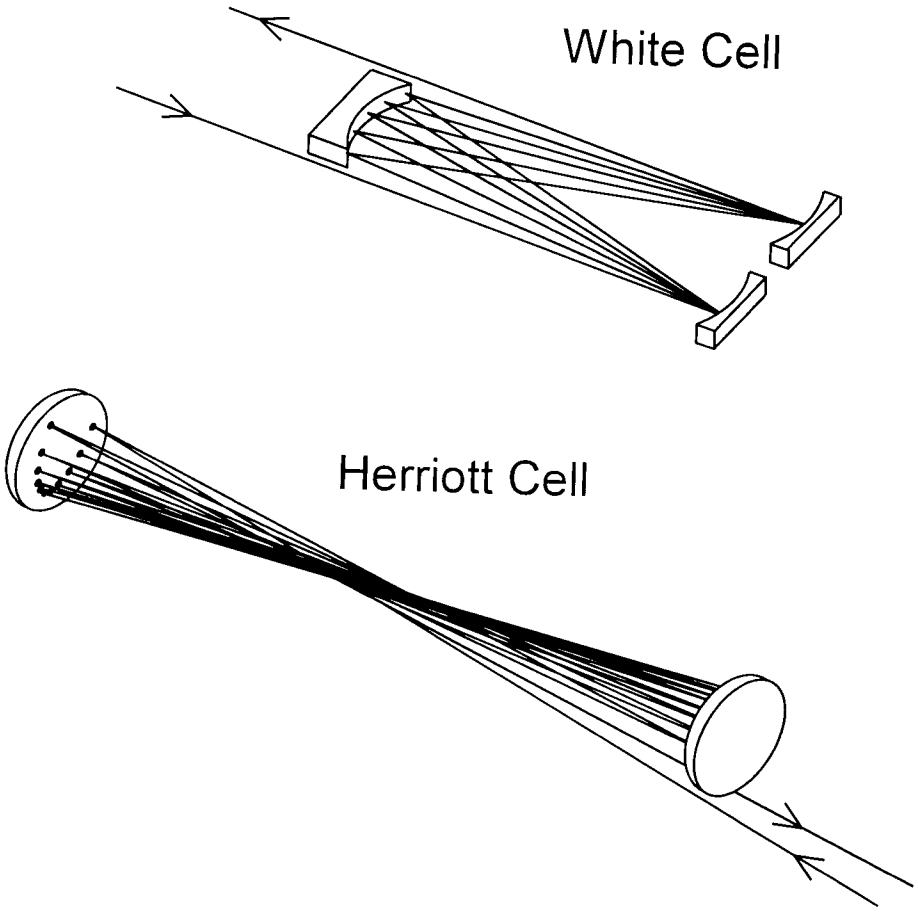

Figure 2.9 Schematic of the two optical configurations used for multipassing the infrared to increase the pathlength.

The laser spots on the entrance/exit mirror for these two multipass cells display qualitatively different behavior. First of all, the equidistant spacing between the spots for the linear pattern in a White cell necessarily requires that with increasing number of passes the clearance between the input/exit beams and the mirror decreases (see Figure 2.10). This is much less the case for the elliptical spot pattern in a Herriott cell, where the spacing between adjacent spots is closest at the "bottom" of the ellipse and steadily increases towards the edge of the mirror. This greatly facilitates cleanly coupling the infrared laser into and out of the multipass optics for the same total number of passes.

Since the entrance/exit mirror in the Herriott cell does not represent a focal plane, one might be tempted to assume that the increased spot size on the mirror will provide a severe limitation on the number of passes achievable without clipping. While an increased spot size could present difficulties, the non Newtonian nature of a Gaussian laser beam provides an effective solution. Specifically, one experimentally observes a variation of spot size with each trip through the multipass(this is not predicted by Newtonian optics, and the magnitude of the variation is directly related to the tightness of the focusing for the incoming beam). This variation can be quantitatively predicted via application of the "ABCD" law for paraxial ray Gaussian optics.[27,28] The two parameters necessary to define a Gaussian beam (TEM_{00}) are the beam spot size, ω, and its radius of phase-front curvature, R. This is often expressed in terms of the complex quantity the beam parameter q:

$$\frac{1}{q} = \frac{1}{R} - \frac{i\lambda}{n\pi\omega^2} \tag{2.8}$$

This is particularly useful in conjunction with a 2×2 matrix charaterization of optical elements and media, where the matrix is denoted:

$$\begin{bmatrix} A & B \\ C & D \end{bmatrix} \tag{2.9}$$

and a series of optical elements is represented by the matrix product of all the constituent pieces. The change in the Gaussian beam upon transmittal through an optical element, or a series of optical elements, is then provided by the ABCD law:

$$q_2 = \frac{Aq_1 + B}{Cq_1 + D} \tag{2.10}$$

The optical elements in the Herriott cell multipass are simply a length free space and two spherical mirrors. The corresponding matrix representation of these elements are:

$$\begin{bmatrix} 1 & d \\ 0 & 1 \end{bmatrix} \tag{2.11}$$

for transmittance through a length d of space and:

$$\begin{bmatrix} 1 & 0 \\ -2/R & 1 \end{bmatrix} \tag{2.12}$$

for reflection off a spherical mirror with radius of curvature R.

The spot sizes determined with this technique for two separate mirror separations are displayed in Figure 2.10. Typically, the mirror separation will be

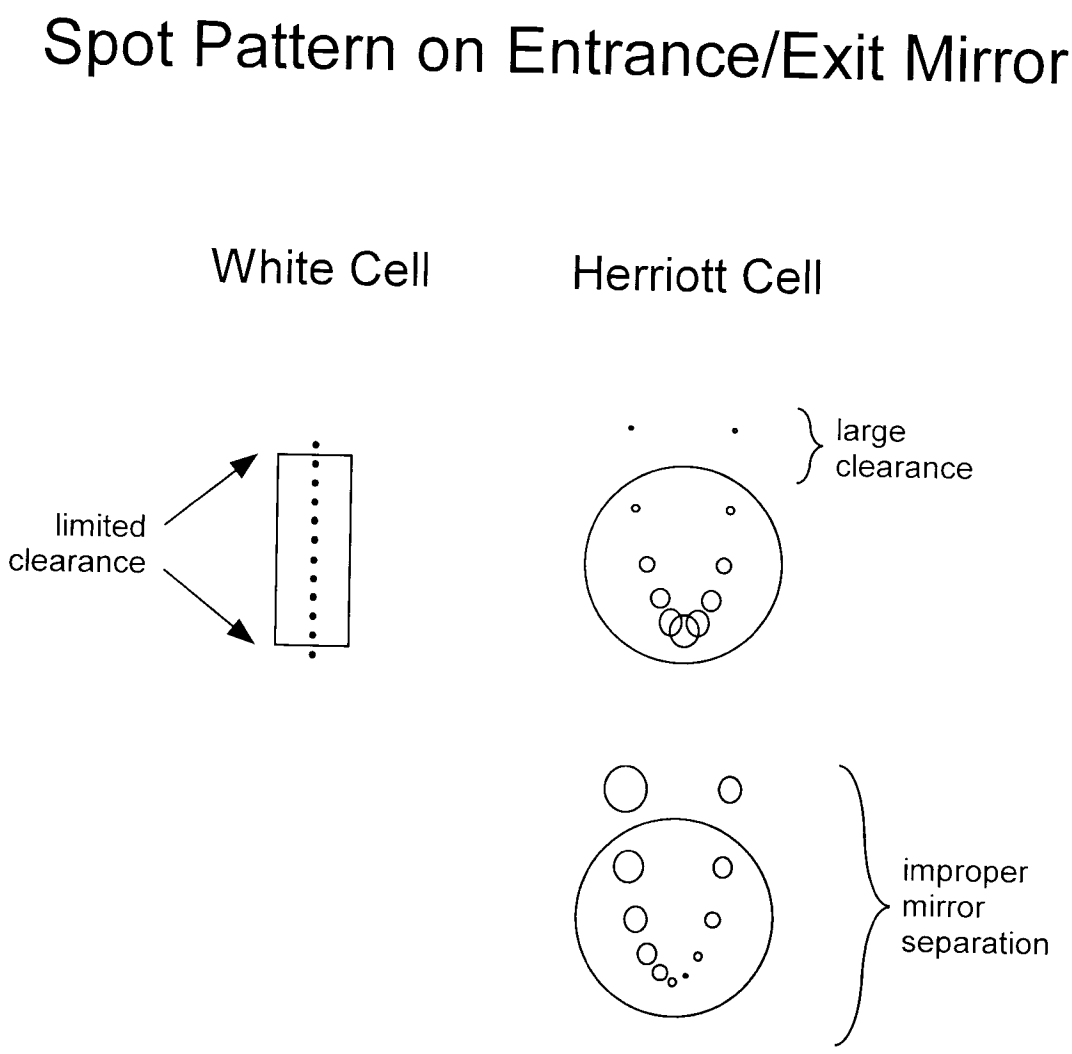

Figure 2.10 Schematic representation of the distribution of spots on the entrance/exit mirror for the two multipass configurations used. The larger clearance provided by the Herriott cell facilitates cleanly coupling into and out of the multipass cell.

tuned to minimize the size of the entrance and exit beam, and therefore reduce the possibility of clipping.

One additional advantage of the Herriott cell vs. the White cell is the decreased expansion region probed. Specifically, a greater number of passes can be clustered closer to the higher density region near the slit orifice. This is of greater value in the studies of monomeric radicals, where the densities drop off inversely with distance from the slit orifice. Furthermore, for the concentration modulation technique described in Chapter 10 the decreased probe region permits higher modulation frequencies.

2.4 Decreasing the Absorption Noise

Direct absorption spectroscopy is the process of detecting small changes (1 part in a million) on a comparatively large background. Unlike zero background experimental techniques (e.g. LIF), any fractional fluctuations in the infrared laser power can be mistaken as a molecular absorption. Therefore extra care must be taken to properly account for any sources of noise. Before discussing some of the techniques employed for noise suppression, however, it is instructive to consider the fundamental limits to absorption sensitivity.

After passing through the slit expansion, the infrared light is detected with a high bandwidth (1 MHz), liquid nitrogen cooled, photovoltaic InSb detector (active area = 0.049 mm^2). The photocurrents are converted to voltages via a 100 kΩ transimpedance amplifier (circuit shown in Figure 2.11). At this stage, even

in the absence of infrared light, two unavoidable noise sources are introduced. The first contribution is the frequency independent resistor noise, or Johnson noise (related to the random motion of electrons in a resistor), and its rms value over a frequency bandwidth Δf in Hz is provided by the equation:

$$V_{Johnson} = (4\, k\, T\, R_s\, \Delta f)^{1/2} \qquad (2.13)$$

where k is Boltzman's constant, and T the absolute temperature of the resistor. For the preamplifier circuit displayed in Figure 2.11, $R_s = 10\ K\Omega$, and therefore the Johnson noise per root bandwidth is 1.3 pA / $\sqrt{Hz}$. The second contribution to the noise arises from the voltage noise of the operation amplifiers used, and is

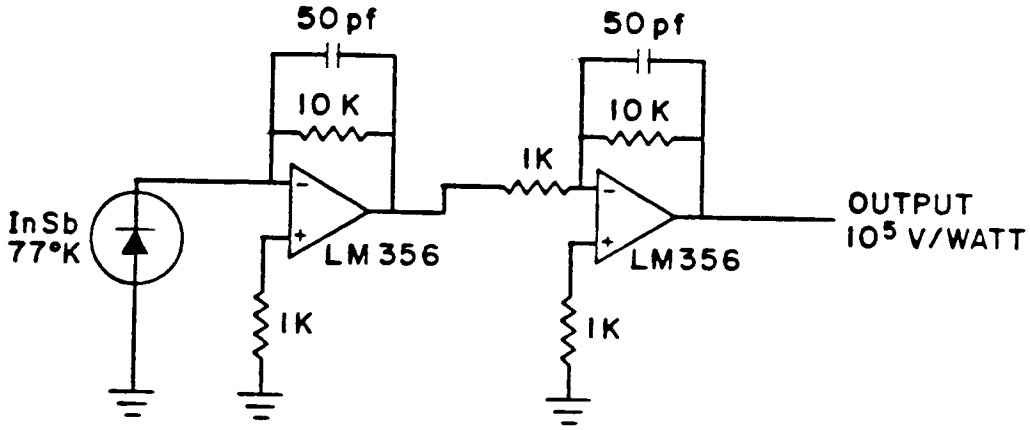

Figure 2.11 The InSb photodiode and transimpedance preamplifier

provided by the manufacturer to be 1.2 pA / $\sqrt{\text{Hz}}$. The total "electronic" noise is then the square root of the sum of squares for these two sources, which is 1.8 pA / $\sqrt{\text{Hz}}$ or equivalently for the 100 kΩ transimpedance, 1.8×10^{-7} V/ $\sqrt{\text{Hz}}$. Displayed in Figure 2.12 is the output of the transimpedance amplifier as viewed by a Hewlett Packard spectrum analyzer. The rms noise of 2.4×10^{-7} V/ $\sqrt{\text{Hz}}$ actually achieved is comparable to our theoretical estimate.

The final "fundamental" source of noise is shot noise, which arises from the discrete nature of the infrared light. The magnitude of this noise is a function of the number of infrared photons (and therefore subsequent number of photovoltaic electrons), and expressed as:

$$i_{shot} = (2\, e\, I_{DC}\, \Delta f)^{1/2} \tag{2.14}$$

where e is the electronic charge in coulombs. For 5 μW of infrared light and 100% quantum efficiency of the InSb, the resultant photocurrent (I_{DC} = 5 μA) translates into an rms shot noise of 1.3 pA / $\sqrt{\text{Hz}}$. Added in quadrature with the other noise sources, and then multiplied by $\sqrt{2}$ to account for the two detectors used (described below), the net total "fundamental" noise is 3.1 pA / $\sqrt{\text{Hz}}$. With respect to the DC photocurrent of 5 μA, this translates into an ultimate absorption sensitivity of 6.2×10^{-7} / $\sqrt{\text{Hz}}$, or for the experimentally used 10 kHz bandwidth, an ultimate achievable absorption sensitivity of 6.2×10^{-5}.

The majority of the noise on the infrared light falls in the low frequency, acoustic region. Requiring the desired infrared absorption to fall in a higher

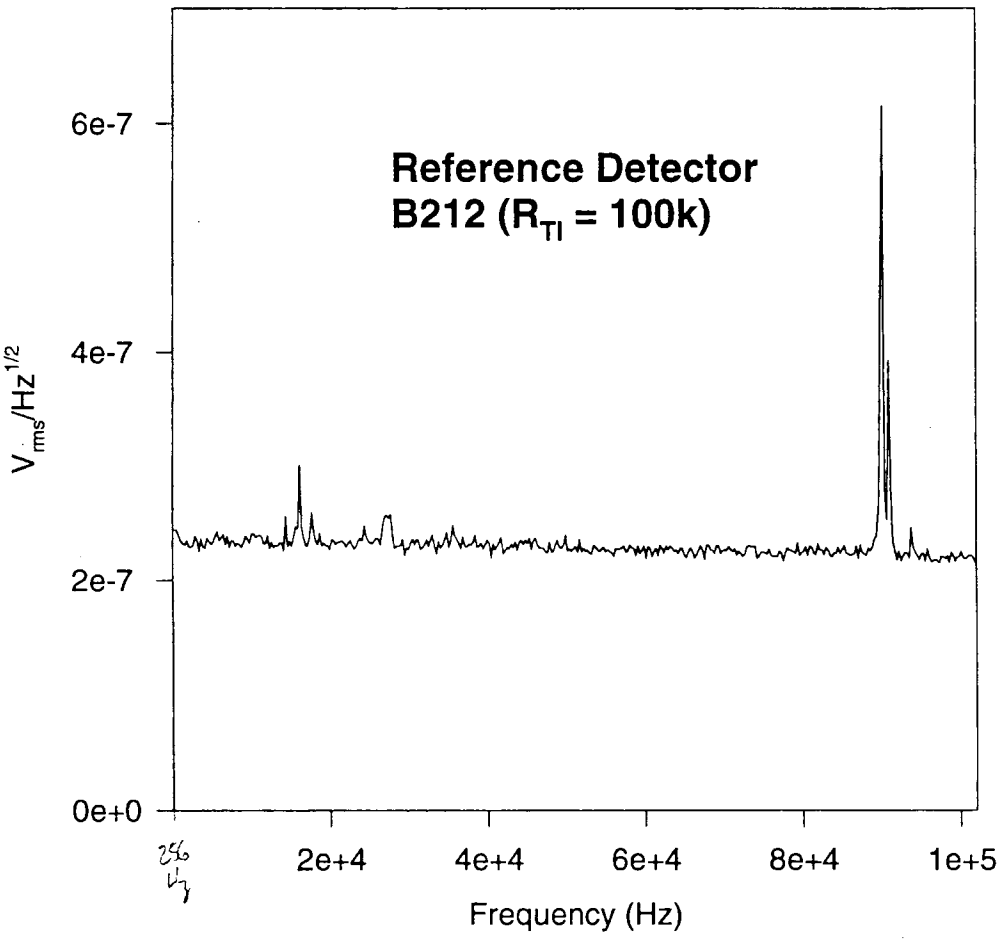

Figure 2.12 Spectral analysis of the intrinsic noise for the InSb / preamplifier combination

frequency region, and then preferentially detecting in this higher region, therefore "bypasses" substantial noise. This was the original motivating factor for undertaking the challenging task of constructing a slit pulsed valve with short temporal pulses (the demands on the pumping speed are a distant second). Specifically, the infrared absorption is filtered with a 3 – 10 kHz longpass and then digitized, synchronously around the valve opening, via a high speed transient digitizer (DSP Technology Model 2001S eight bit digitizer and summer, with a 1 MHz, adjustable up to 100 MHz, sample rate). The digitized wave form is transferred to the computer as an array, and then divided into three parts: two baseline gates and one signal gate, as shown in Figure 2.13. In the figure both the offset and the slope of the temporal absorption have been exaggerated to emphasize the role played by the baseline gates. Specifically, summation over the signal gate alone provides the sum of the areas for the regions marked A and B on the figure. For small absorptions (unlike what is shown in the figure), the area of region B can be comparable to or even larger than the area of A. Therefore, determination and subtraction of region B is necessary.

The two baseline gates are summed, and then normalized to their length, NC_1 and NC_2. The difference between these normalized sums ($NC_2 - NC_1$), divided by the distance between the centers of the two gates ($t_4 - t_1$) provides the slope of the baseline, $S_{baseline}$. Linear interpolation to points t_2 and t_3 then yields

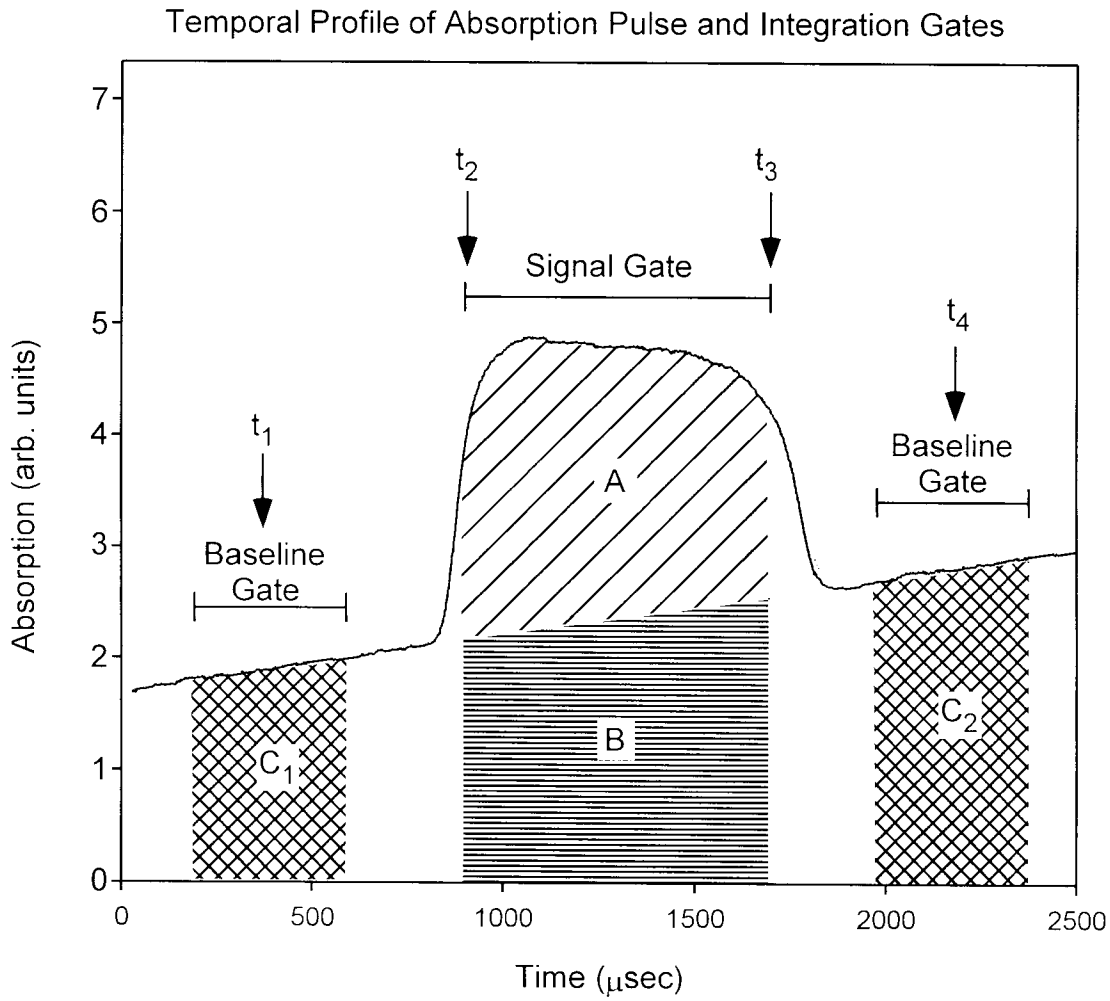

Figure 2.13 A Sample time profile corresponding to infrared absorption during the opening of the pulsed valve. The integrated areas of the hatched regions are provided by summation over the different integration gates. The baseline gates provide the volume of region B, which then allows extraction of the desired region A.

the dimensions of region B and therefore extraction of region A from the integrated signal gate. The area of region A is then normalized by the length of the signal gate and stored. Simultaneous storing of the infrared power permits subsequent conversion to percent absorption. Both the length and positions of all three regions are fully adjustable. This integration scheme effectively filters out low frequency fluctuations in the baseline.

An additional technique for suppression of common mode noise on the infrared laser is provided by a signal minus reference subtraction. Prior to entering the vacuum chamber, the infrared light is split into two paths (see Figure 2.1). The signal path probes the long axis of the slit supersonic expansion prior to detection with an InSb detector. The reference beam is detected with a separate matched InSb detector. Subtraction of these two beams, in principle, eliminates common mode noise on the infrared laser. Noise reductions from 30 to 50 fold are regularly achieved.

Due to the different optical pathlengths, varying frequency response of the infrared beam splitter, and other factors, prior to subtraction the relative intensity of the two beams need to be adjusted to optimize noise cancellation. This was traditionally done via manual adjustment of a voltage divider until the rms fluctuations of the subtracted signal, as viewed on an oscilliscope, are minimized. This technique requires continual user supervision during the course of a scan. Recently implemented is an electronic servo, which automatically adjusts the relative intensity of the signal and reference beam prior to subtraction. Shown in Figure 2.14 is the circuit diagram. The assay for adjusting the relative signal to

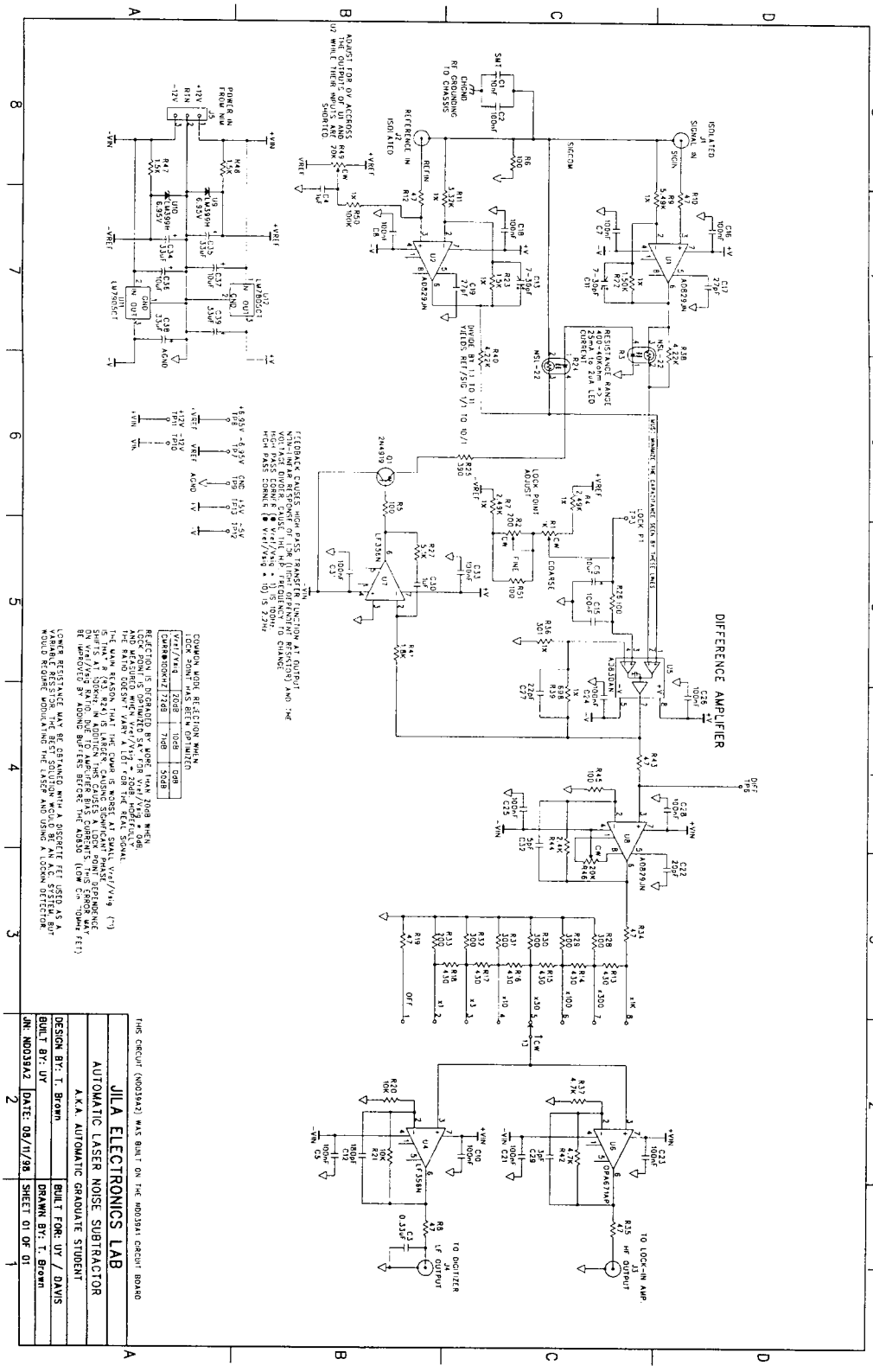

Figure 2.14 Circuit diagram for the automatic laser noise subtractor.

reference beam intensity is simply a measure of the two beams dc components. The electronic attenuation of the infrared signal is accomplished via a light dependent resistor (ldr). Since the $LiNbO_3$ oven produces a significant dc offset which differs for the two detectors, a manually adjusted offset is required. While servoing on the relative DC components of the two beams might seem foolish, especially since it is the higher frequency components which one cares about, nevertheless this circuit works remarkably well. In the limit of complete failure of the electronic servo loop, manual adjustment of the offset provides the identical convenience of the older subtraction circuit.

References for Chapter 2

1 C. M. Lovejoy, M. D. Schuder, and D. J. Nesbitt, *Journal of Chemical Physics* **85,** 4890-4902 (1986).

2 C. M. Lovejoy and D. J. Nesbitt, *Journal of Chemical Physics* **86,** 3151-3165 (1987).

3 C. M. Lovejoy and D. J. Nesbitt, *Review of Scientific Instruments* **58,** 807-811 (1987).

4 E. Riedle, S. H. Ashworth, J. T. Farrell, Jr., and D. J. Nesbitt, *Review of Scientific Instruments* **65,** 42-48 (1994).

5 J. T. Farrell, Jr., S. Davis, and D. J. Nesbitt, *Journal of Chemical Physics* **103,** 2395- (1995).

6 J. T. J. Farrell, PhD, University of Colorado, 1995.

7 A. McIlroy, , University of Colorado, 1991.

8 M. D. Schuder, , University of Colorado, 1991.

9 C. M. Lovejoy, *Ph.D. thesis, University of Colorado* (1990).

10 R. W. Boyd, *Nonlinear Optics* (Academic Press, Boston, 1992).

11 P. N. Butcher and D. Cotter, *The Elements of Nonlinear Optics* (Cambridge University Press, Cambridge, 1990).

12 A. S. Pine, *Journal of the Optical Society of America* **64,** 1683-1690 (1974).

13 R. Balhorn, H. Kunzmann, and F. Lebowsky, *Applied Optics* **11,** 742 (1972).

14 T. M. Niebauer, J. E. Faller, H. M. Godwin, J. L. Hall, and R. L. Barger, *Applied Optics* **27,** 1285-1289 (1988).

15 P. Lee and M. Skolnick, *Applied Physics Letters* **10,** 303 (1967).

16 J. L. Hall and S. A. Lee, *Applied Physics Letters* **29,** 367-369 (1976).

17 B. Stahlberg, P. Jungner, and T. Fellman, *Optics and Laser Technology* **22,** 146-149 (1990).

18 L. Oudejans, K. Nauta, and R. E. Miller, *Journal of Chemical Physics* **105,** 10410 (1996).

19 A. S. Pine, *Journal of Molecular Spectroscopy* **82,** 435 (1980).

20 T. A. Dixon, C. H. Hoyner, F. A. Baiocchi, and W. Klemperer, *Journal of Chemical Physics* **74,** 6539-6543 (1981).

21 S. Davis, J. J. Farrell, D. T. Anderson, and D. J. Nesbitt, *Chemical Physics Letters* **256,** 157-162 (1995).

22 W. B. Olson, *Applied Optics* **23,** 1580-1585 (1984).

23 J. V. White, *Journal of the Optical Society of America* **32,** 285-288 (1942).

24 D. Herriott, H. Kogelnik, and R. Kompfner, *Applied Optics* **3,** 523-526 (1964).

25 D. R. Herriott and H. J. Schulte, *Applied Optics* **4,** 883-889 (1965).

26 D. Kaur, A. M. de Souza, J. Wanna, S. A. Hammad, L. Mercorelli, and D. S. Perry, *Applied Optics* **29,** 119-124 (1990).

27 J. H. Moore, C. C. Davis, and M. A. Coplan, *Building Scientific Apparatus* (Addison-Wesley Publishing Company, New York, 1989).

28 Amnon Yariv, Optical Electronics, (Oxford University Press, Oxford, 1991).